electronics

Article

A Novel Non-Resonant Full-Bridge Multi-Output Topology for Domestic Induction Heating Applications

Sezer Aslan [1,2,*], Ulas Oktay [1,2] and Nihan Altintas [1]

[1] Department of Electrical Engineering, Yildiz Technical University, Esenler, Istanbul 34220, Turkey; ulas.oktay@beko.com (U.O.); naltin@yildiz.edu.tr (N.A.)
[2] Central R&D Department, Beko Corporate, Tuzla, Istanbul 34950, Turkey
* Correspondence: sezer.aslan@std.yildiz.edu.tr or sezer.aslan@beko.com

Abstract: Induction heating technology plays a significant role in heating applications with its high efficiency, fast response, and precise control ability. Traditional resonant inverter-based systems face problems such as complexity, lack of flexibility, and low efficiency in multi-load situations. To overcome these issues, a new non-resonant full-bridge multiple-output inverter topology using silicon carbide (SiC) semiconductor devices is presented. While the system is simplified by eliminating resonant components, efficiency is increased thanks to SiC devices. In the study, a coil design methodology focusing on coil resistance and inductance is presented to optimize energy transfer and maximize system performance. Load-sensing and advanced frequency-modulation techniques are integrated to provide precise and independent power regulation in multi-loads. Thus, the efficiency of energy distribution and system robustness are increased. The proposed topology offers heating performance that provides homogeneous heat distribution. The developed prototype was proven to operate reliably with high efficiency under different load conditions and was suitably applied for domestic induction heating applications. An efficiency of 96.78% was achieved at a 50 kHz operating frequency and 2000 W power level.

Keywords: domestic induction heating; multi-output inverter; non-resonant multi-output induction heating topology

Academic Editors: Kai Fu and Jingyang Fang

Received: 17 December 2024
Revised: 22 January 2025
Accepted: 1 February 2025
Published: 3 February 2025

Citation: Aslan, S.; Oktay, U.; Altintas, N. A Novel Non-Resonant Full-Bridge Multi-Output Topology for Domestic Induction Heating Applications. *Electronics* **2025**, *14*, 596. https://doi.org/10.3390/electronics14030596

1. Introduction

Induction heating (IH) technology is extensively used in industrial, domestic, and medical applications because of its high efficiency, rapid heating, precise temperature control capability, and enhanced safety [1,2]. IH technology, which was first introduced in the 1970s for domestic applications, directly transfers heat to cookware, resulting in improved energy efficiency and user safety [3–5]. It is also widely preferred in industrial applications for its reliability, and in medical applications for controlled heating of biomedical implants and hyperthermia treatments [6–8]. Such features, including the versatility and reliability of IH, make it a more efficient, controllable, and safer alternative to conventional heating methods, supporting a wide range of applications [9].

Traditional IH systems are commonly used due to their efficiency and rapid heating capabilities, especially in domestic applications. Typically, IH systems have an AC-DC rectifier connected to a resonant inverter stage, with Single Switch Quasi-Resonant (SSQR), half-bridge series resonant (HBSR), and full-bridge topologies being popular choices. Out of these, HBSR, with its higher power efficiency and easier control, is widely used. SSQR focuses on the design requirements for low-cost applications, while full-bridge inverters are used for high-power applications [9–12].

Modern IH systems are designed based on user demands for flexible cookware sizes, shortened cooking durations, and increased power requirements (Figure 1). Such requirements according to which they have been forced to develop multi-output structures and flexible cooking surfaces [13], which allow for better versatility and comfort. Flexible cooking surfaces accommodate different cookware dimensions, reduce cooking times, and maximize energy use, reflecting the changing demands of the users [14].

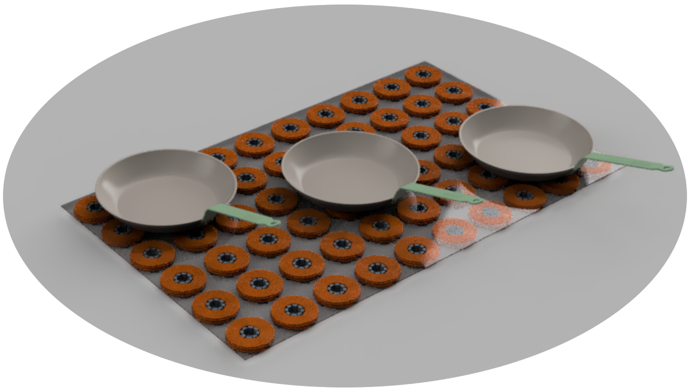

Figure 1. A common flexible multi-output induction cooker.

In addition to advancements in zone control systems, multi-output topologies in IH systems are gaining importance for balancing cost, performance, and complexity. These topologies can be classified into three main approaches: single-output inverter parallelization, load multiplexation, and multi-output inverters, as shown in Figure 2 [15].

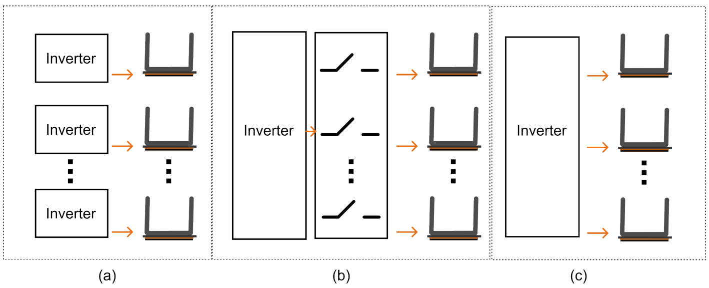

Figure 2. Classification of multi-output power converters for IH loads: (**a**) single-output inverter parallelization, (**b**) load multiplexation, (**c**) multi-output inverters.

Using separate single switch Class E inverters in the single-output parallelization method addresses the simplicity and low-cost issue of multi-coil systems [16]. Perfect for low power applications, this solution also significantly lessens interference, enabling coils to work independently (induction cookers usually have 2–4 hobs). Standard resonant inverters, including the full-bridge (FB), half-bridge (HB), and single-ended zero-current switching topologies [17–19], are commonly used in these systems. As the number of coils increases, the scalability of the circuits is limited due to intermodulation noise. Additionally, the increase in coils leads to a reduction in the availability of soft switching, further complicating the system's efficiency. Although leveraging existing inverter designs eases implementation and allows for strong modulation, the linear growth of power devices causes increased weight and cost, and switching frequency limitations prevent independent load control. Hence, this approach is relatively desirable only for systems with a small number of IH loads [20].

The second method is load multiplexation, where the same inverter is connected to several coils via a relay-based multiplexing network [21]. In this method, the inverter manages multiple IH loads using modulation schemes such as variable switching frequency and time-averaged activation of the loads. It is a very common approach since it is efficient and easy to implement. However, it has certain disadvantages, including noise, slow switching speed, limited relay lifespan, and the need for a complex load identification process. To overcome these limitations, a combined topology of two inverters with a half-wave rectifier has been presented [22]. In each HB inverter, it is connected to a mains half cycle, and a second inverter is used to manage relay reconfiguration [20,23–25].

Meanwhile, use of a multi-output inverter is an alternative method which uses a single converter to activate multiple coils at the same time and has proven to be more reliable and versatile to work with. It is the most advanced solution, with multi-load control and frequency selection, and ideal high-power requirements. However, it is not without notable challenges in complexity and cost. To overcome the limitations of low-frequency load multiplexing in relay-based systems, various multi-output topologies have been developed. These designs reduce the number of components, simplify the inverter structure, and increase versatility, making the method more practical and widely applicable [26–30]. HB topologies with frequency selection are commonly used in parallel IH systems to activate certain loads and form the resonant tanks with separated frequencies. Nevertheless, significant challenges remain, driven by the wide variability in switching frequencies and the inherent complexities of non-ideal impedance pathways. Proposals to solve these challenges come in the form of using an FB inverter with different switching frequencies, or cascaded resonant converters for multi-coil systems for more independent power control [28,31]. Although direct AC-AC multi-inverters and dual-output full-bridge converters improve control flexibility, they face efficiency and complexity trade-offs as the number of coils increases [32–35]. Newer configurations, such as series resonant multi-inverters utilizing 900-V SiC MOSFETs C3M0065090D (Wolfspeed, Durham, NC, USA), can effectively decrease switching losses and use pulse-density modulation (PDM) to minimize electromagnetic interference. However, challenges related to high-precision control and load management persist in practical applications [13].

In recent years, non-resonant inverters have emerged as a viable alternative to conventional resonant topologies for IH applications. Such topologies can provide cost benefits by reducing the number of components needed, even removing resonant capacitors while allowing designs to be smaller and more robust [36,37]. Phase-shift modulation (PSM) and other pulse patterns are then used to efficiently control the output power, achieving up to 96.8% efficiency. However, they also have a few drawbacks, including lower output power for half-bridge inverters caused by lower coil voltage and higher switching power losses in pulse-width modulation (PWM) [37]. The proposed topology involves a non-resonant multi-output half-bridge inverter [36] for flexible cooking surfaces that is increasingly flexible as multiple inductors can be applied in parallel operation, permitting the usage of diverse pot sizes and placements.

The high-voltage and high-frequency operation of semiconductors makes wide band gap (WBG) semiconductor devices such as silicon carbide (SiC) and gallium nitride (GaN) attractive for modern power electronics. Switching and conduction losses of SiC devices make them suitable for higher energy efficiency applications, e.g., domestic IH. Moreover, their high switching speed enables the design of compact, high-efficiency systems [13,38,39]. In contrast, GaN devices exhibit higher switching speeds with very low transition losses, which are especially beneficial in low-voltage applications, perfectly matching the requirements of space-efficient and energy-efficient IH systems [40–42].

This paper presents a compact and efficient non-resonant full-bridge multiple-output inverter topology utilizing SiC semiconductor devices for high-performance domestic IH applications. By leveraging the flexibility of non-resonant configurations and SiC technology, the topology effectively powers multiple parallel-connected loads with varying power requirements. Fully integrated SiC devices reduce switching and conduction losses, support high-frequency operation, and minimize cooling needs and coil size. The elimination of resonant elements simplifies control, using frequency modulation (FM) and PDM for precise power control and selective load activation, enhancing efficiency. Zero-voltage switching (ZVS) further minimizes switching losses and improves overall performance. An optimized coil design ensures efficient energy transfer, uniform heat distribution, and homogeneous heating, while load detection through coil current and DC bus voltage enables accurate pan recognition for optimal power transfer and maximum system efficiency.

2. The Proposed Non-Resonant Full-Bridge Multi-Output Topology

The induction cooker draws energy from the mains voltage, which is rectified using a bridge diode. This process is followed by the use of a bus filter to handle significant voltage ripples, ensuring an input power factor close to unity [20]. An inverter, employing either a resonant or non-resonant topology, then generates high-frequency current to supply the induction coil, enabling efficient heating. This overall operational flow is illustrated in Figure 3.

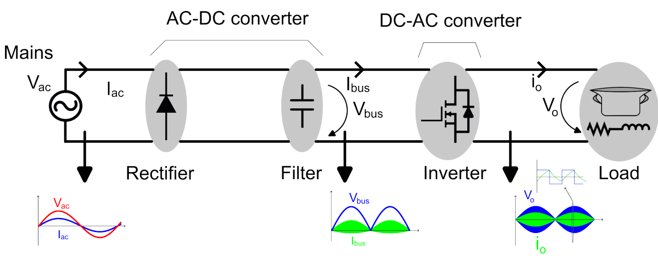

Figure 3. General block diagram representation of an induction cooker system.

In this section, the proposed topology will be presented along with its operating ranges, waveforms, load power control, and coil design details.

2.1. Topology

The full-bridge non-resonant multi-output inverter topology proposed in this study is illustrated in Figure 4. The circuit is composed of two primary blocks. The first block is a full-bridge circuit constructed using SiC-based semiconductors, which are optimized for high efficiency and switching performance. The second block, referred to as the load branch, includes four SiC diodes and a Si IGBT (S_{axk}) to manage the connection and disconnection of the load. The load is modeled with $R_{eq,k}$ and $L_{eq,k}$, representing its resistive and inductive characteristics.

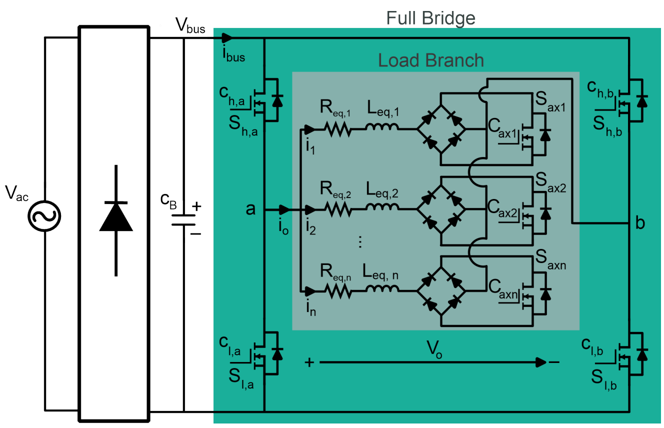

Figure 4. The proposed non-resonant full-bridge multi-output topology and the load branch.

A capacitor C_B is integrated into the system to stabilize the input voltage and suppress ripples. This capacitor minimizes voltage fluctuations and ensures reliable system operation. In branch 'a', switches $S_{h,a}$ and $S_{l,a}$ operate as high-side and low-side switches, respectively. Similarly, in branch 'b', switches $S_{h,b}$ and $S_{l,b}$ fulfill the same roles. The voltages at the midpoints of the branches, V_a and V_b, alternate between V_{bus} and zero, enabling the necessary switching behavior for efficient energy transfer.

The body diodes of the switches conduct during freewheeling intervals, enabling switching transitions under zero-voltage conditions ZVS. This reduces switching losses, increases system efficiency, and allows for higher switching speeds.

Figure 5 depicts the basic equivalent circuits corresponding to switching states I–IV when the first load is activated within the shared inverter block. During this operation, the control signal C_{ax1} is applied, enabling energy delivery to the load branch. It is assumed that the voltage across the V_{CB} terminals remains constant during a single operation period of the circuit, and the input section is represented as a constant DC source in equivalent intervals.

Figure 6 illustrates the fundamental circuit intervals corresponding to t_0, t_1, t_2, t_3, and t_4, providing a detailed representation of the switching dynamics.

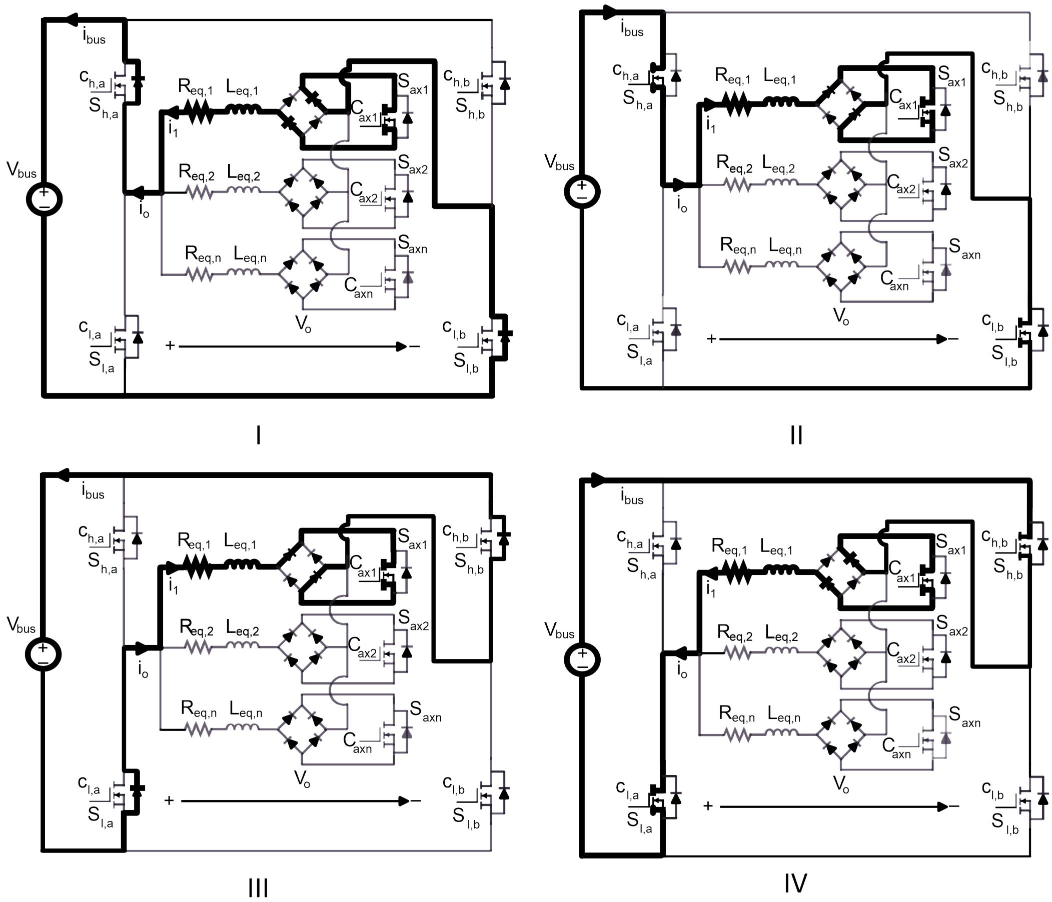

Figure 5. The proposed non-resonant full-bridge multi-output topology corresponds to the equivalent circuit intervals of (**I–IV**).

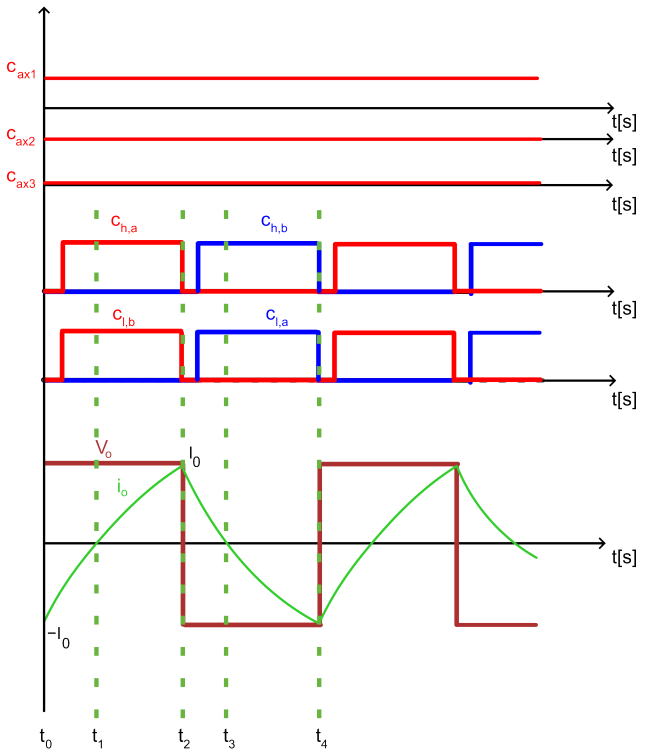

Figure 6. General waveforms of the proposed non-resonant full-bridge multi-output topology.

Interval I (t_0–t_1): This interval begins with the switching off of $S_{h,b}$ and $S_{l,a}$. During this interval, the diodes associated with $S_{h,b}$ and $S_{l,a}$ conduct to maintain current flow. During this interval, the control signals $C_{h,a}$ and $C_{l,b}$ are applied, ensuring ZVS operation when the parallel diodes of $S_{h,a}$ and $S_{l,b}$ are conducting.

In the first interval, the initial current in the circuit is assumed to be $-I_0$. Accordingly, the circuit equation (Equation (1)) is derived using Kirchhoff's Voltage Law (KVL):

$$V_{bus} = L_{eq,1}\frac{dI_1(t)}{dt} + R_{eq,1}I_1(t) \tag{1}$$

In this equation, V_{bus} represents the supply voltage of the circuit, $L_{eq,1}$ is the inductance, and $R_{eq,1}$ is the resistance. The characteristic equation is solved to obtain the homogeneous solution for the current I_h, given as Equation (2):

$$I_h(t) = Ke^{-\frac{R_{eq,1}}{L_{eq,1}}t} \tag{2}$$

The particular solution for the current is determined as $I_P = \frac{V_{bus}}{R_1}$. The general solution is expressed as the sum of the homogeneous and particular solutions (Equation (3)):

$$I(t) = I_h(t) + I_p = Ke^{-\frac{R_{eq,1}}{L_{eq,1}}t} + \frac{V_{bus}}{R_{eq,1}} \tag{3}$$

Using the initial condition $(I(0) = -I_0)$, the constant K is calculated as shown in Equation (4):

$$I(0) = K + \frac{V_{bus}}{R_{eq,1}} = -I_0 \quad \Rightarrow \quad K = -I_0 - \frac{V_{bus}}{R_{eq,1}} \tag{4}$$

As a result, the current equation is expressed as shown in Equation (5):

$$I(t) = \left(-I_0 - \frac{V_{bus}}{R_{eq,1}}\right)e^{-\frac{R_{eq,1}}{L_{eq,1}}t} + \frac{V_{bus}}{R_{eq,1}} \tag{5}$$

Interval II (t_1–t_2): The switches $S_{h,a}$ and $S_{l,b}$ are in conduction mode, and the current path includes $S_{h,a}$, $R_{eq,1}$, $L_{eq,1}$, the full-bridge diode, $S_{ax,1}$, and $S_{l,b}$, completing the circuit.

The same equations derived in Interval I (Equations (1)–(5)) are valid in this interval, with the initial condition appropriately adjusted. According to this equation, the exponential rate of increase in the current diminishes over time, asymptotically approaching the value of $\frac{V_{BUS}}{R_1}$ as time progresses.

Interval III (t_2–t_3): This interval begins with removing the control signals of switches $S_{h,a}$ and $S_{l,b}$. During this interval, the current path transitions through the body diodes of $S_{h,b}$ and $S_{l,a}$. This interval concludes when the current becomes zero. During the conduction period of the diodes, the control signals for the switches $S_{h,b}$ and $S_{l,a}$ can be applied.

In this interval, the initial current is assumed to be I_0. Kirchhoff's Voltage Law is applied, yielding the same circuit equation as in Interval I:

$$V_{bus} = L_{eq,1}\frac{dI_1(t)}{dt} + R_{eq,1}I_1(t) \tag{6}$$

The homogeneous and particular solutions remain unchanged $I_P = -\frac{V_{bus}}{R_1}$, leading to the general solution:

$$I(t) = I_h(t) + I_p = Ke^{-\frac{R_{eq,1}}{L_{eq,1}}t} - \frac{V_{bus}}{R_{eq,1}} \tag{7}$$

Using the initial condition $(I(0) = I_0)$, the constant K is calculated as follows:

$$I(0) = K - \frac{V_{bus}}{R_{eq,1}} = I_0 \quad \Rightarrow \quad K = I_0 + \frac{V_{bus}}{R_{eq,1}} \tag{8}$$

Thus, the current equation is expressed as:

$$I(t) = \left(I_0 + \frac{V_{bus}}{R_{eq,1}}\right)e^{-\frac{R_{eq,1}}{L_{eq,1}}t} - \frac{V_{bus}}{R_{eq,1}} \tag{9}$$

Interval IV (t_3–t_4): With the reversal of current direction, the switches $S_{h,b}$ and $S_{l,a}$, which were activated in the previous interval, start conducting the current. The switches $S_{h,b}$ and $S_{l,a}$ operate under ZVS conditions, and the current flows through $S_{h,b}$, $R_{eq,1}$, $L_{eq,1}$, the full-bridge diode, $S_{ax,1}$, and $S_{l,a}$, completing the circuit. The same equations derived in Interval III (Equations (6)–(9)) are valid here, with the initial condition properly adjusted.

Non-resonant and resonant inverter topologies offer different advantages in applications such as IH systems. The use of WBG semiconductor devices reduces switching losses in non-resonant topologies, improving efficiency and enabling simpler circuit designs without the need for resonant components. The presence of resonant elements and the need for precise frequency tuning can complicate the circuit design. Therefore, the advantages and disadvantages of both topologies should be evaluated based on application requirements.

The proposed non-resonant full-bridge multi-output topology is an induction cooker design that offers a multi-output configuration. Each output branch contains four diodes and an auxiliary switch, enabling flexible power distribution and independent control of different loads. One of the advantages of the non-resonant design is the elimination of resonant elements, which reduces circuit complexity and cost. Furthermore, this topology is compatible with WBG semiconductors, providing high-efficiency operation. With these features, it offers a flexible and modular power distribution solution, making it suitable for a wide range of applications.

2.2. Load Sensing

This section provides a detailed explanation of the load-sensing methodology implemented in the proposed non-resonant full-bridge multi-output topology for IH. This critical technique is designed to detect the presence and position of various loads (such as pots or pans) on the cooker surface. By optimizing power transfer for each output branch, load sensing ensures energy is supplied only to the necessary areas, enhancing the efficiency and performance of the cooker. This method begins by sampling the inductor current and the DC bus voltage over a single period. Subsequently, the sampled current values are analyzed using the Discrete Fourier Transform (DFT) to extract the coefficients of the first harmonic. The sampled DC bus voltage is then transformed into the lower IGBT voltage form by considering the snubber capacitances. A DFT is applied to this transformed voltage for the first harmonic. The resistance (R) and inductance (L) values are calculated by dividing the voltage value by the current.

Step 1: Apply the DFT to the current sampled over one period with N samples. Here, h represents the harmonic index, n denotes the sample index, and $a_{v,h}$ and $b_{v,h}$ are the cosine and sine coefficients of the h-th frequency component of $v_o(n)$, respectively.

$$I(h) = \frac{1}{N}\sum_{n=0}^{N-1}\left[i(n)\left(\cos\left(2\pi\frac{hn}{N}\right) - j\sin\left(2\pi\frac{hn}{N}\right)\right)\right] = a_{i,h} - jb_{i,h} \tag{10}$$

Step 2: Transform V_{bus} into V_o as illustrated in Figure 4, then apply the DFT to V_o.

$$V_o(h) = \frac{1}{N}\sum_{n=0}^{N-1}\left[v_o(n)\left(\cos\left(2\pi\frac{hn}{N}\right) - j\sin\left(2\pi\frac{hn}{N}\right)\right)\right] = a_{v,h} - jb_{v,h} \tag{11}$$

Step 3: Compute the values of R and L for the first harmonic using the formulas provided below.

$$R_h = \frac{a_{v,h}a_{i,h} + b_{v,h}b_{i,h}}{a_{i,h}^2 + b_{i,h}^2} \tag{12}$$

$$L_h = \frac{1}{\omega_h}\frac{a_{v,h}b_{i,h} - b_{v,h}a_{i,h}}{a_{i,h}^2 + b_{i,h}^2} \tag{13}$$

$$\omega_h = 2\pi f_h \tag{14}$$

Using Equations (12) and (13), load detection becomes feasible based on the sampled DC bus voltage and inductor current.

2.3. Modulation Strategies and Power Control

In the non-resonant full-bridge topology, a PDM technique synchronized with the main grid is used to control the loads [39]. This modulation strategy selectively activates and deactivates loads to achieve the desired average power levels.

The Modulation Ratio (m_k) in PDM control defines the ratio of a load's activation time to its total operation time. This ratio determines the pulse density required to achieve a specific power level. As the activation ratio for a load increases, its average output power also rises; conversely, a modulation ratio results in reduced power:

$$m_k = \frac{t_{on,k}}{T_{PDM}} \tag{15}$$

where $t_{on,k}$ and T_{PDM} represent the activation time of the k-th load and the total period, respectively.

PDM enables precise control of output power while reducing electromagnetic interference (EMI), harmonic distortion, and potential switching losses by ensuring that switching events occur at zero-crossing instances of the grid voltage. By sequentially selecting and activating the loads, the pulse density is adjusted at specific intervals according to the total power demand, allowing for individual load management and balancing power fluctuations. The PDM control method is applied to the auxiliary switches, which activate or deactivate the connected loads based on control signals. This approach ensures that all timing parameters are synchronized to the multiples of the half-cycles of the grid frequency, contributing to more energy-efficient switching operations, minimizing power losses, and reducing thermal stress on the devices [13,43].

Figure 7 [13] illustrates output load current and voltage waveforms, and the PDM technique's pulse-density modulation waveforms.

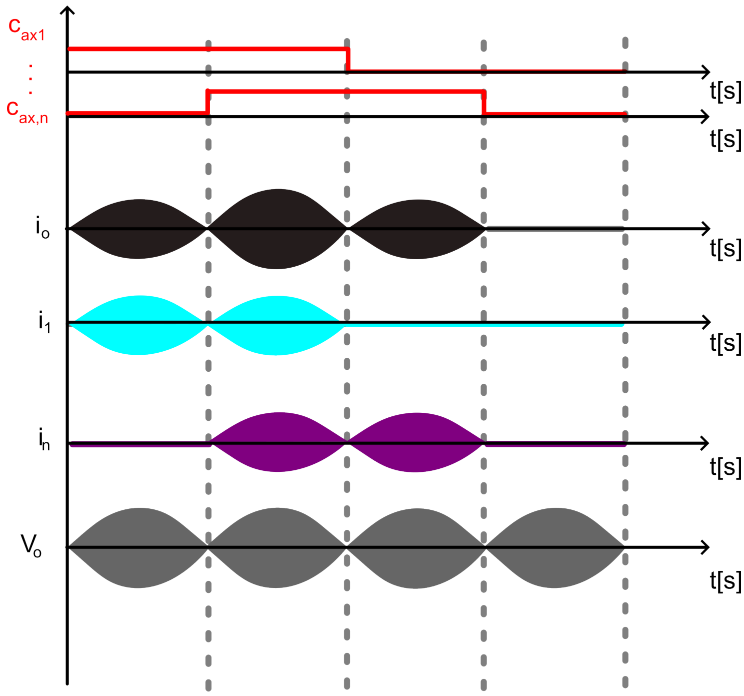

Figure 7. Waveforms of the modulation strategy for power control.

2.4. Coil Design

The analysis of the inductor must account for both the transient and steady-state intervals. In Figure 8, the waveform of the inductor current is presented, illustrating its transient and steady-state behaviors.

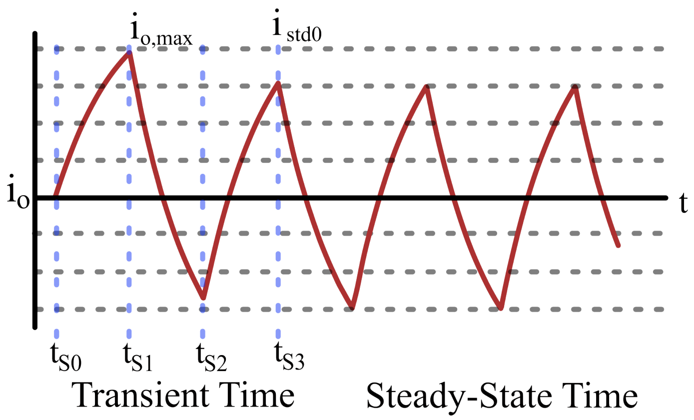

Figure 8. Transient and steady-state conditions of the coil current.

When determining the inductance of the coil, the minimum inductance value is calculated under no-load conditions. Using the maximum current $i_{o,\max}$ and V_o as input parameters at t_{s1}, the inductance is determined according to Equation (16).

$$i(t) = \frac{V_o}{L} t \tag{16}$$

In a steady state, the maximum current is denoted as $i_{\mathrm{stdo,max}}$. Since the waveform of the current changes is in a steady state, the resistance value must be recalculated based on the steady-state power. The RMS current in a steady state is determined using Equation (16), and the power level is verified using Equation (20). I_{std0} represents the initial value of the steady-state current, while V_{stdo} denotes the output voltage at a steady state. The coil and pot system is typically represented by an electrical model consisting of an R-resistor, an L-inductor, and a P-power term.

The maximum and minimum current values in the steady state are determined iteratively by using the current range equations until the values converge, ensuring the steady-state conditions are satisfied.

$$A = I_{std0}^2 R^2 - 2 I_{std0} R V_{stdo} + V_{stdo}^2 + 4 V_{stdo} (I_{std0} R - V_{stdo}) e^{\frac{R(t_{S3} - t_{S2})}{L}} \tag{17}$$

$$B = \left(I_{std0}^2 R^2 + 2 I_{std0} R V_{stdo} - 3 V_{stdo}^2 \right) e^{2 \frac{R(t_{S3} - t_{S2})}{L}} \tag{18}$$

$$I_{\mathrm{stdo,rms}} = \frac{\sqrt{2}}{2} \cdot \sqrt{\frac{-L(A - B) e^{-2 \frac{R(t_{S3} - t_{S2})}{L}}}{R(t_{S3} - t_{S2})} + \frac{2 V_o^2}{R^2}} \tag{19}$$

The initial resistance value is calculated using Equation (20):

$$R_{\mathrm{initial}} = \frac{V_{stdo}^2}{P} \tag{20}$$

The steady-state power is verified using Equation (21):

$$P = {I_{\mathrm{stdo,rms}}}^2 R \tag{21}$$

If the measured power surpasses the target value, the resistance is decreased; conversely, if the power falls short of the target, the resistance is increased. This iterative procedure continues until the steady-state current $I_{\mathrm{stdo,rms}}$ and power level satisfy the specified requirements. Furthermore, Figure 9 presents an algorithm for inductor design, utilizing critical parameters such as input power, operating frequency, maximum output current, and output voltage.

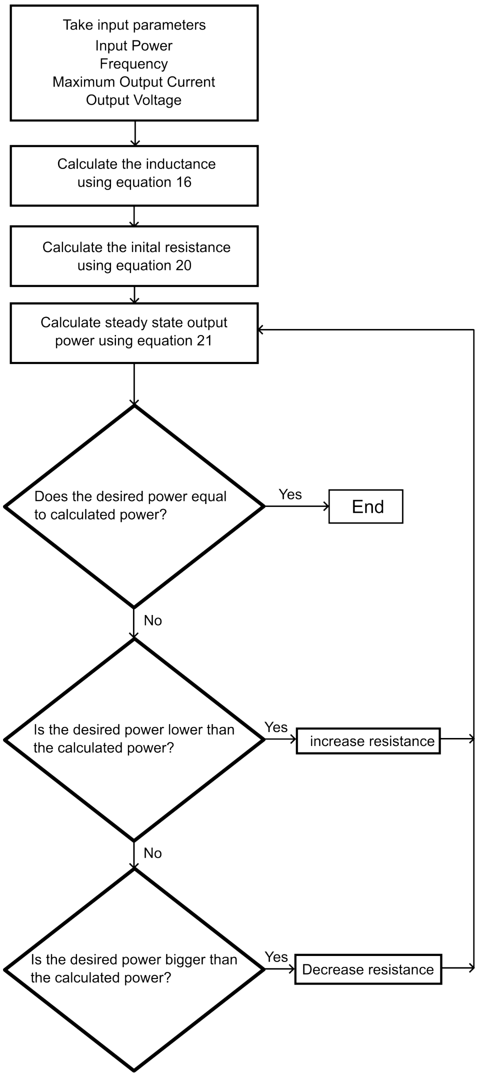

Figure 9. Flowchart of the inductor design algorithm.

3. Implementation

To assess the feasibility and performance of the proposed converter, an experimental prototype was designed and developed. This section provides an overview of the main implementation and experimental results.

3.1. Prototype

An experimental prototype, as illustrated in Figure 10, was designed and constructed to validate the applicability of the proposed topology and modulation strategies for IH applications.

Table 1 summarizes the input parameters used for designing the coil. These parameters include the power (P) of 670 W per load (2010 W total for three loads) and the design of three coils to support the three loads.

Table 1. Input parameters for designing coil.

Parameters	Input Parameters' Explanation	Value
P	Power	670 W × 3 (2010 W)
F	Frequency	50 kHz
$I_{o,max}$	Maximum output current	33.24 A
V_o	Output voltage	226 V

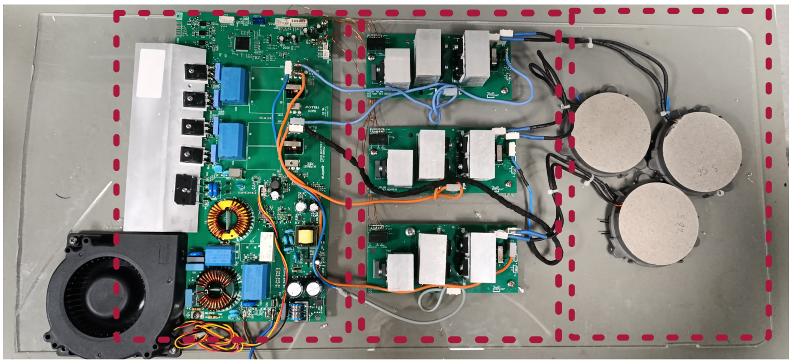

Figure 10. Test board and environment for topology validation.

The simulation setup and results were systematically analyzed to validate the performance of the induction heating system. Table 2 summarizes the parameter determination of the FEM simulation, including operating conditions and boundary definitions. The results primarily focus on the distribution of magnetic flux density.

Table 2. Summary of FEM simulation parameters and aspects.

Parameters and Aspects	Single Coil Details	Triple Coil Details
Parameter determination (Resistance (R), Inductance (L))	R = 8 Ω, L = 68 µH Power = 670 W.	Parameters for individual coils remain the same; total power = 2010 W
Operating conditions	Power = 670 W Current = 18 A Frequency = 50 kHz.	Total power = 2010 W Total current = 54 A Frequency = 50 kHz
Coil current and frequency	Sinusoidal current of 18 A peak, 50 kHz.	Sinusoidal current distributed across three coils (54 A total)
Analysis convergence	Mesh density = 1.72%.	Mesh density = 1.72%
Boundary conditions	Vacuum environment; domain size large enough to avoid flux distortion.	Same as single coil
Current excitation	Direct sinusoidal current applied (18 A, 50 kHz).	Total sinusoidal current distributed across coils (54 A, 50 kHz)

As shown in Figure 11, the system's performance was analyzed under various operating conditions. These scenarios provide insights into the magnetic interactions and flux distribution when coils operate individually or collectively.

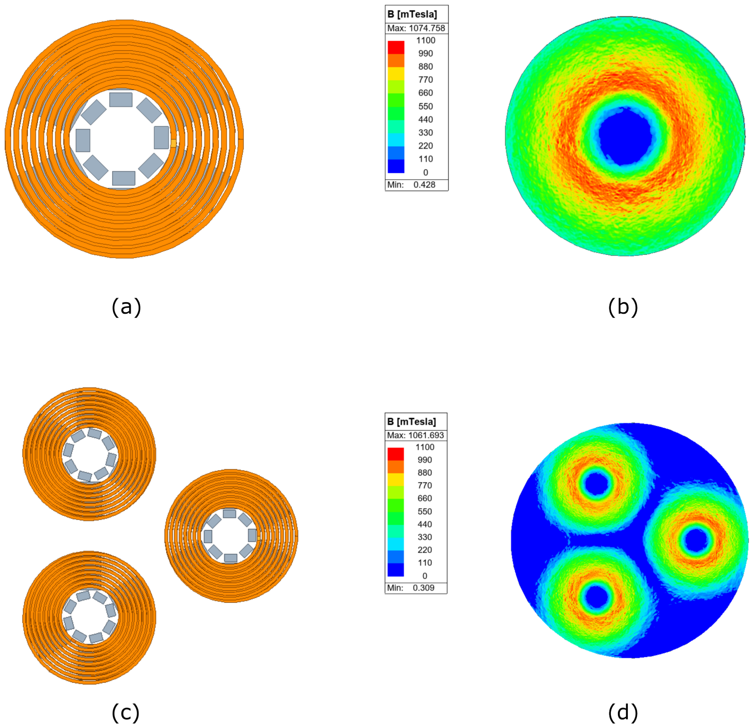

Figure 11. Performance analysis of the proposed system under various operating conditions for the 670 W coil with $R = 8\ \Omega$ and $L = 68\ \mu$H: (**a**) Operation with a single active coil, (**b**) flux distribution during single-coil operation, (**c**) operation with all three coils active, and (**d**) flux distribution with all three coils active.

The converter system is managed by an MCU-based digital control architecture, which generates PWM signals for each power component. The MCU is integrated with a PC via USB and serial protocols, allowing direct adjustments of modulation parameters through the PC interface. The flow of the control algorithm, as illustrated in Figure 12, is depicted as follows: The system begins by sampling the DC bus voltage (v_{bus}), the output current (i_o), and individual load currents (i_1, i_2, i_3) using ADCs. The sampled data are processed to detect the active loads through the load detection block. Based on the detected load conditions, the frequency and modulation index (m_k) are calculated. Control signals are then generated for the auxiliary signals and the main full-bridge gate drivers, which manage the operation of Load1, Load2, and Load3. The zero-cross detector synchronizes the system with the mains voltage, while a PI controller ensures stable operation by adjusting the system parameters to meet desired performance metrics.

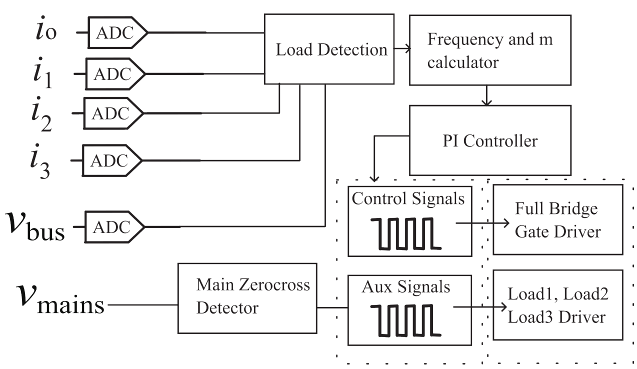

Figure 12. Proposed non-resonant full-bridge multi-output control methodology.

For the non-resonant full-bridge induction cooker topology, the IMW120R020M1H SiC MOSFET was selected. This MOSFET offers as follows:

- A voltage rating of 1200 V and a current rating of 98 A.
- A low $R_{DS(on)}$ value of 19 mΩ, ensuring minimal conduction losses and high efficiency.
- A gate threshold voltage of 4.2 V, offering immunity to parasitic turn-on events, and compatibility with a 0 V gate-off voltage.

The device's robust body diode allows for high performance in hard-commutation scenarios, while its .XT interconnection technology maximizes thermal performance, making it suitable for demanding full-bridge applications. In the load branches, SiC diodes (WNSC5D30650W) and Si IGBTs, (IHW40N65R6) were utilized to optimize power transfer. The prototype is configured to supply power to three 670 W loads with induction loads characterized by $L = 68$ μH and $R = 8$ Ω connected in parallel.

3.2. Experimental Results and Comparison

This section presents a detailed experimental evaluation of the proposed converter system. The analysis starts with an examination of control signals and switching waveforms to illustrate the system's operational behavior and energy transfer dynamics. This is followed by an exploration of various load coverage scenarios, demonstrating the system's adaptability to different operating conditions and its ability to effectively manage energy distribution across multiple outputs. The results confirm the reliability and practicality of the system in diverse applications.

The primary experimental measurements of the proposed converter system are detailed below. A set of tests was conducted for three loads, capable of delivering output power between 180 W and 670 W. For simplicity, only results obtained for three loads are presented, which can be generalized to systems with more loads.

P_{in} represents the input power. The power values are illustrated in Figure 13, highlighting their dependency on frequency and modulation control. Specifically, an increase in frequency results in a decrease in power output, while a reduction in the modulation index (m_k) leads to a linear decrease in power transfer. The m_k graph in Figure 13 provides a detailed representation of the power ratios based on these parameters.

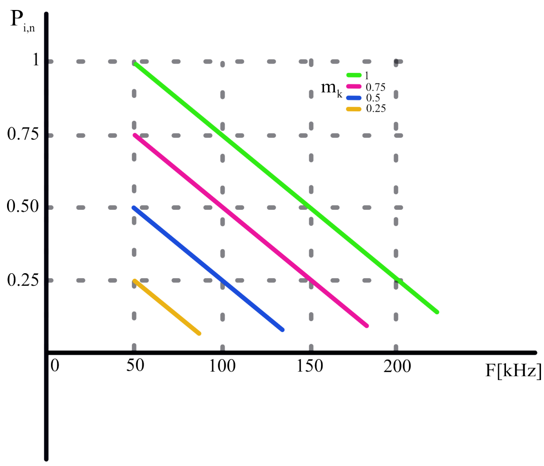

Figure 13. Power values based on frequency and modulation control.

3.2.1. Control Signal and Switching Waveforms

The experimental results demonstrate the performance of the proposed system under varying conditions. Figures 14–16 illustrate critical aspects such as current flow, switching characteristics, and control signal behaviors at different power levels. These waveforms provide a comprehensive insight into the operational dynamics, energy dissipation, and ZVS conditions achieved in the converter.

Figure 14a illustrates the flow of current ($I_{sl,a}$) through the shared component ($S_{l,a}$), while Figure 14b presents the detailed turn-off switching characteristics, and Figure 14c depicts the turn-on switching characteristics. As shown in Figure 14b, hard switching occurs during the turn-off process, with the power loss in the switch (P_{loss}) plotted using the oscilloscope's math function. This provides a clear representation of energy dissipation during this interval. The switch current was measured using a Rogowski current probe, while the drain and gate voltages were measured with a passive voltage probe. To ensure alignment between the current and voltage waveforms, the deskew value provided in the Rogowski current probe datasheet (17 ns) was applied during the measurement, and the passive probe was compensated accordingly. During the turn-on process, it is observed from Figure 14c that the switch ($S_{l,a}$) operates under ZVS, as the control signal is applied while the body diode is conducting. The turn-off process represents the transition from Interval IV to Interval I, while the turn-on process corresponds to the transition from Interval III to Interval IV.

The waveforms in Figure 15 verify the converter's proper operation by showing the load control system's dynamic behavior. It illustrates the control signal, switch voltage, and current when power is transferred to the first branch, with (m_1 = 0.33) and 221 W output power. In this condition, the main branch current equals the sum of the currents in the active branches. Increasing the signal width raises (m_1), enhancing the transferred power.

In Figure 16, the current, voltage, and control signals of the proposed converter are depicted for two different power levels: (a) 2000 W at a frequency of 50 kHz, and (b) 550 W at a frequency of 190 kHz. In both load conditions, with all three branches active, the control signals for the switches are applied while their body diodes are conducting, ensuring that the switches transition to conduction under ZVS conditions.

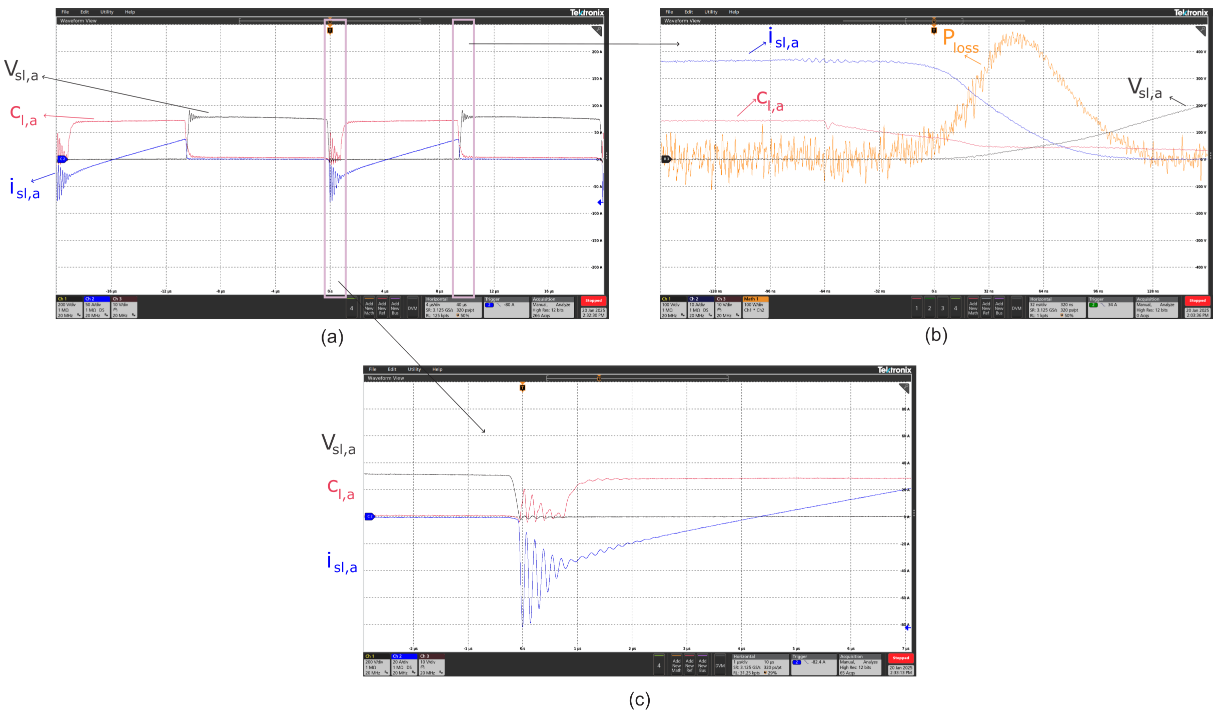

Figure 14. (**a**) Flow of current $I_{sl,a}$ through the shared component ($i_{sl,a}$: 50 A/div, $V_{sl,a}$: 200 V/div, $c_{l,a}$: 10 V/div, time: 4 µs/div), (**b**) turn-off characteristics ($I_{sl,a}$: 10 A/div, $V_{sl,a}$: 100 V/div, $C_{l,a}$: 10 V/div, time: 32 ns/div), and (**c**) turn-on characteristics under ZVS conditions ($I_{sl,a}$: 20 A/div, $V_{sl,a}$: 200 V/div, $C_{l,a}$: 10 V/div, time: 1 µs/div).

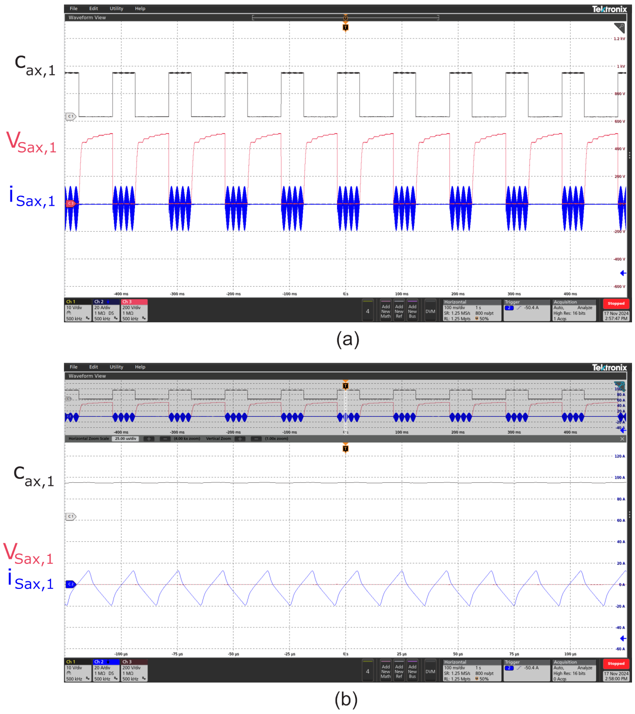

Figure 15. (**a**) Switch control signal voltage and current for the auxiliary signal ($C_{ax,1}$: 10 V/div, $V_{sax,1}$: 200 V/div, $I_{sax,1}$: 20 A/div, time: 100 ms/div), (**b**) detailed oscilloscope display showcasing a zoomed-in region ($C_{ax,1}$: 10 V/div, $V_{sax,1}$: 200 V/div, $I_{sax,1}$: 20 A/div, time: 5 µs/div).

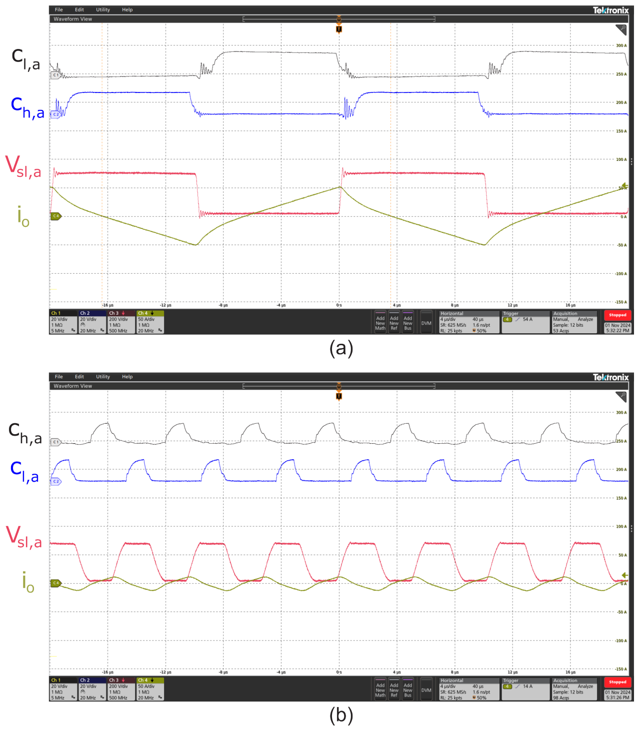

Figure 16. Current, voltage, and control signals of the proposed converter for two different power levels with all three loads active: (**a**) 2000 W at 50 kHz, (**b**) 550 W at 190 kHz ($C_{l,a}$: 20 V/div, $C_{h,a}$: 20 V/div, $V_{sl,a}$: 200 V/div, i_o: 50 A/div, time: 4 µs/div).

3.2.2. General Operation Waveforms

An overview of the system's operation under various coverage scenarios, demonstrating its flexibility and performance, is provided in Figure 17a,b, depicting a specific partial coverage scenario, while Figure 17c represents the full coverage scenario, where all three coils are active and delivering maximum power, Figure 17d shows a partial coverage scenario with varied power levels for each load, Figure 17e,f demonstrate additional partial coverage scenarios with different power distributions, and Figure 17g illustrates a scenario with lower power levels for all loads. Finally, Figure 17h depicts a partial coverage scenario where only one coil operates at full capacity while the others remain inactive. These scenarios evaluate the modulation strategies at different power levels and highlight the system's ability to adapt to varying operational conditions.

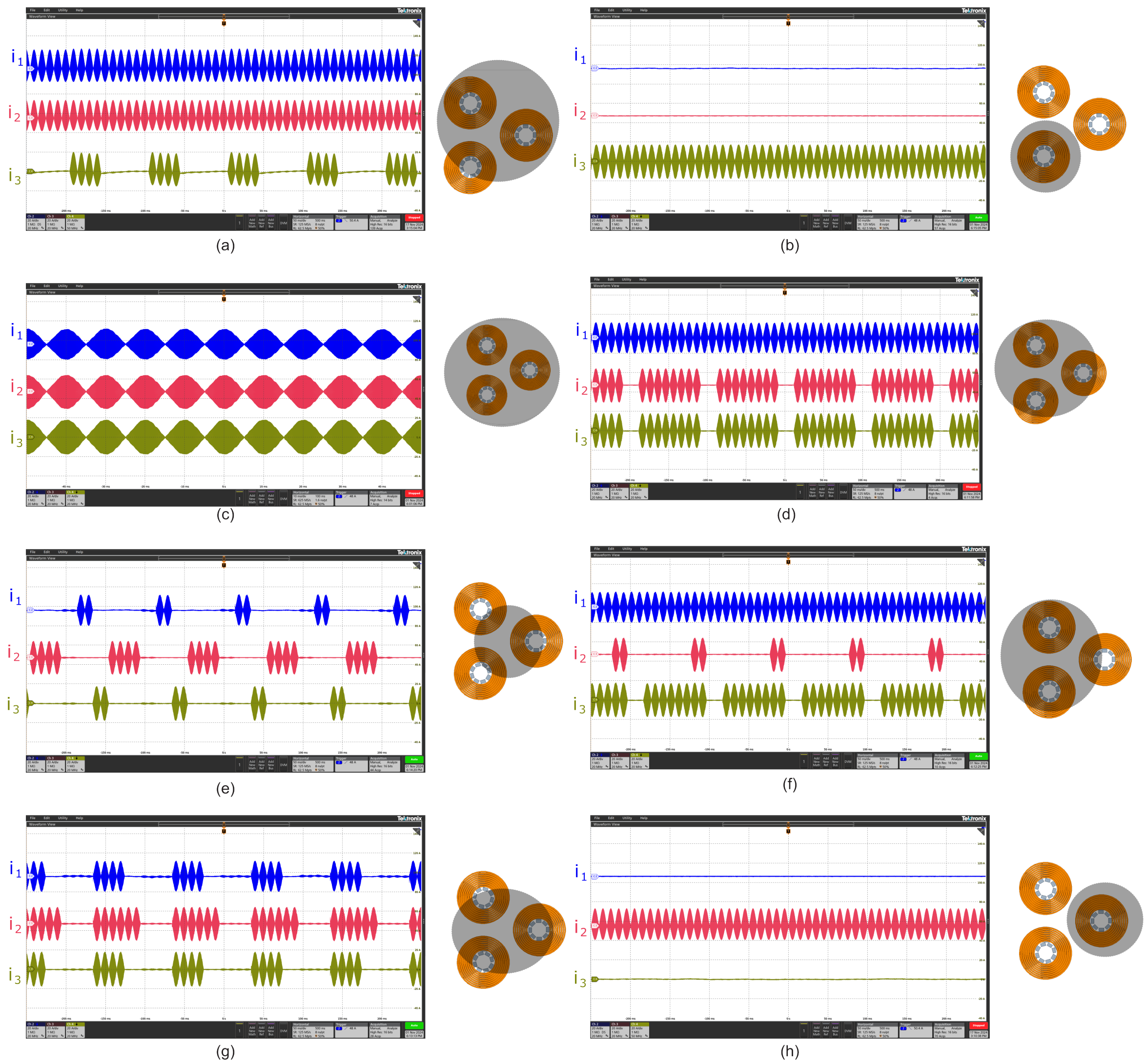

Figure 17. Coverage scenarios: (**a**) Partial coverage scenario ($m_1 = 1, 670$ W; $m_2 = 1, 670$ W; $m_3 = 0.33$, 221 W), (**b**) partial coverage scenario ($m_1 = 0, 0$ W; $m_2 = 0, 0$ W; $m_3 = 1, 670$ W), (**c**) full coverage scenario with maximum power delivery ($m_1 = 1, 670$ W; $m_2 = 1, 670$ W; $m_3 = 1, 670$ W), (**d**) partial coverage scenario ($m_1 = 1, 670$ W; $m_2 = 0.83, 550$ W; $m_3 = 0.83, 550$ W), (**e**) partial coverage scenario ($m_1 = 0.17, 114$ W; $m_2 = 0.33, 221$ W; $m_3 = 0.17, 114$ W), (**f**) partial coverage scenario ($m_1 = 1, 670$ W; $m_2 = 0.17, 114$ W; $m_3 = 0.83, 550$ W), (**g**) partial coverage scenario ($m_1 = 0.25, 168$ W; $m_2 = 0.42$, 282 W; $m_3 = 0.33, 221$ W), and (**h**) partial coverage scenario ($m_1 = 0, 0$ W; $m_2 = 1, 670$ W; $m_3 = 0$, 0 W). For all cases, i_1, i_2, i_3: 20 A/div, with time scales of 50 ms/div (**a**,**b**,**d**–**h**) and 10 ms/div (**c**).

Experimental visuals, such as those illustrating the presence of a load on the coil, can further support the analysis by showcasing the practical implementation and successful energy transfer in real-world scenarios.

3.2.3. Efficiency Measurements Results

In order to find the efficiency of the proposed topology, the circuit is operated at different power values. The efficiency curve is given in Figure 18. The input power is measured using YOKOGAWA WT500 (Yokogawa Electric Corporation, Tokyo, Japan) (accuracy: ±0.1%), while the output power is calculated by multiplying I_o and V_o, which are measured using the Rogowski coil (CWT Ultra-mini (Power Electronic Measurements Ltd., Nottingham, UK), accuracy: ±2%) and the MSO54 oscilloscope (Tektronix, Beaverton, OR, USA) (accuracy: ±1%), respectively. The combined uncertainty of the measurement system is calculated to be approximately ±2.24%. The efficiency is then determined as the ratio between the output and input power, considering this combined uncertainty. It is observed that the efficiency reaches up to 96.78% under full-load conditions, where the output is fully powered, with a measurement uncertainty of ±2.24%.

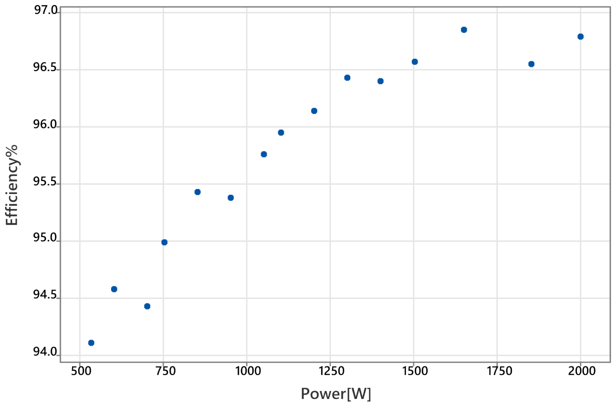

Figure 18. Experimental efficiency analysis of the proposed non-resonant multi-output full-bridge topology.

The current and voltage waveforms of the components were measured using an oscilloscope to calculate the losses. The difference between the input and output power, after subtracting the switching losses, is defined as other component losses. These include losses that cannot be directly measured, such as inductor losses and conduction losses in the paths. The total power loss distribution in the proposed non-resonant multi-output full-bridge topology, including contributions from the Si IGBTs, SiC diodes, SiC MOSFETs, and other components, is presented in Figure 19. As shown, under maximum load conditions, the highest power loss occurs in the other components, followed by the SiC diodes and Si IGBTs, with the SiC MOSFETs contributing the least to the total power loss.

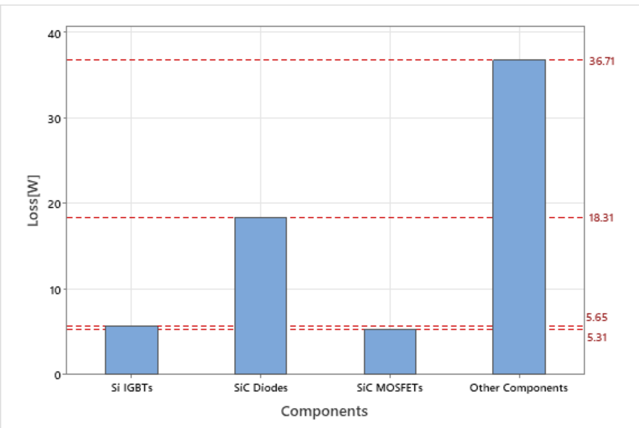

Figure 19. Total power loss distribution in the proposed non-resonant multi-output full-bridge topology, including contributions from Si IGBTs, SiC diodes, SiC MOSFETs, and other components losses under maximum load conditions.

3.2.4. Comparison and Discussion

In this study, a comparison has been made between the non-resonant multi-output topology, commonly found in the literature, and the full-bridge series resonant multi-inverter, which is a closely related resonant topology. The analysis focuses on their respective designs, operational characteristics, and suitability for different power conversion applications to highlight the advantages and limitations of each approach.

The proposed topology, the non-resonant multi-output half-bridge inverter, and the full-bridge series resonant multi-inverter differ significantly in their design and component requirements, as presented in Table 3, as well as in their control techniques, output power, and switching frequency, as shown in Table 4. The proposed topology eliminates the need for relays, simplifying the system compared to the non-resonant topology, which relies on two relays for switching. On the other hand, the full-bridge series resonant multi-inverter, being resonant in nature, requires an additional resonant capacitor for each load, which increases both design complexity and component count. These distinctions highlight the varying trade-offs and application suitability of each topology.

Table 3. Comparison of inverter topologies in terms of component counts.

Topology	Transistor	Relay	Diode
Non-resonant multi-output half-bridge inverter [36]	$2n + 2$	2	0
Full-bridge series resonant multi-inverter [13]	$4 + n$	0	0
Proposed topology	$4 + n$	0	4

n is the number of load.

The proposed topology, the non-resonant multi-output half-bridge inverter, and the full-bridge series resonant multi-inverter use distinct control techniques optimized for their designs and applications. The non-resonant multi-output half-bridge inverter uses phase-shifted modulation (PSM) and frequency modulation (FM), which are simple but can be challenging for independent control with multiple inductors due to magnetic interactions. The full-bridge series resonant multi-inverter employs PSM, FM, and PDM, offering flexibility but requiring precise tuning and synchronization for resonant circuits. The proposed topology avoids resonant components, effectively utilizing SiC diodes in high-frequency stages to suppress switching losses and Si IGBTs in low-frequency load stages to achieve improved cost-performance efficiency.

Table 4. Comparison of inverter topologies in term of difference aspects.

Topology	Control	Output Power	Switching Frequency
Non-resonant multi-output half-bridge inverter	PSM, FM	828 W	100–500 kHz
Full-bridge series resonant multi-inverter	PSM, PDM, FM	700 W	146–240 kHz
Proposed topology	PDM, FM	2010 W	50–190 kHz

4. Conclusions

In this study, a novel non-resonant full-bridge multi-output inverter topology employing SiC semiconductor devices was developed for domestic induction heating applications. The proposed design introduces flexible and independent power control capabilities to domestic induction heating systems while ensuring high efficiency. Precise control of each load was achieved through advanced load-sensing techniques and frequency-modulation methods.

Experimental studies validated the performance of the prototype through tests conducted under eight different load scenarios. The test results demonstrated that the proposed topology ensures precise power distribution across multiple outputs and uniform heat distribution across the heating surface, enabling homogeneous heating. The system efficiency under these scenarios has been provided to highlight the design's performance. The utilization of the PDM strategy allowed for selective activation of loads, reducing power losses and enhancing overall system effectiveness. The proposed topology achieved an efficiency of 96.78% at an operating frequency of 50 kHz and a power level of 2000 W, showcasing its high-performance capabilities in domestic induction heating applications.

The proposed topology eliminates the need for resonant components by leveraging SiC diodes in high-frequency stages to minimize switching losses while utilizing Si IGBTs in low-frequency load stages to optimize cost-performance efficiency. This study presents a user-oriented solution that offers independent load management and flexible operation, making it a high-performance and innovative option for domestic induction heating applications.

Author Contributions: Conceptualization, S.A. and N.A.; methodology, S.A. and N.A.; software, S.A.; validation, S.A.; investigation, S.A. and U.O.; resources, S.A.; data curation, S.A. and N.A.; writing—original draft preparation, S.A.; writing—review and editing, S.A. and N.A.; visualization, S.A. and U.O.; supervision, N.A. All authors have read and agreed to the published version of the manuscript.

Funding: This research received no external funding.

Data Availability Statement: Data are contained within the article.

Acknowledgments: We would like to acknowledge the partial use of OpenAI's ChatGPT 4o language model for assisting in language editing and format refinement of this manuscript. The model's contributions were limited to improving readability and formatting, while all technical content and scientific interpretations were solely developed and verified by the authors. This work was supported by BEKO CORPORATE, which provided the necessary resources and expertise to facilitate the successful completion of this study.

Conflicts of Interest: Authors S.A. and U.O. were employed by the company Beko Corporate. The remaining author, N.A., declares that the research was conducted in the absence of any commercial or financial relationships that could be construed as potential conflicts of interest.

Abbreviations

The following abbreviations are used in this manuscript:

IH	Induction Heating
SiC	Silicon carbide
SSQR	Single Switch Quasi-Resonant
HBSR	Half-bridge series resonant
SE-ZCS	Single-Ended Zero-Current Switching
ZVS	Zero-Voltage Switching
QR	Quasi-Resonant
PDM	Pulse-density modulation
WBG	Wide Band Gap
GaN	Gallium nitride
PSM	Phase-shifted modulation
PWM	Pulse-width modulation
ADC	Analog to Digital Converter

References

1. Lucia, O.; Maussion, P.; Dede, E.J.; Burdio, J.M. Induction Heating Technology and Its Applications: Past Developments, Current Technology, and Future Challenges. *IEEE Trans. Ind. Electron.* **2014**, *61*, 2509–2520. [CrossRef] [CrossRef]
2. Chen, X.; Wang, J.; Ma, B.; Duan, Z.; Wang, H. Research Status and Applications of Dual-Frequency Induction Heating Power Supply. *Electronics* **2024**, *13*, 4913. [CrossRef] [CrossRef]
3. Moreland, W.C. The Induction Range: Its Performance and Its Development Problems. *IEEE Trans. Ind. Appl.* **1973**, *IA-9*, 81–85. [CrossRef] [CrossRef]
4. Ozturk, M. A Simplified Design Method for Quasi-Resonant Inverter Used in Induction Hob. *Electronics* **2023**, *12*, 4145. [CrossRef] [CrossRef]
5. Altuntaş, H.; Arslan, M.S. A New Approach for Infrared Temperature Measurement Sensor Systems and Temperature Control for Domestic Induction Hobs. *Sensors* **2025**, *25*, 235. [CrossRef] [CrossRef] [PubMed]
6. Xu, Q.; Ma, F.; Luo, A.; Chen, Y.; He, Z. Hierarchical Direct Power Control of Modular Multilevel Converter for Tundish Heating. *IEEE Trans. Ind. Electron.* **2016**, *63*, 7919–7929. [CrossRef] [CrossRef]
7. Stauffer, P.R.; Cetas, T.C.; Jones, R.C. Magnetic Induction Heating of Ferromagnetic Implants for Inducing Localized Hyperthermia in Deep-Seated Tumors. *IEEE Trans. Biomed. Eng.* **1984**, *BME-31*, 235–251. [CrossRef] [CrossRef]
8. Di Barba, P.; Dughiero, F.; Sieni, E. Synthesizing Distributions of Magnetic Nanoparticles for Clinical Hyperthermia. *IEEE Trans. Magn.* **2012**, *48*, 263–266. [CrossRef] [CrossRef]
9. Zungor, F.; Bodur, H.; Ozturk, M.; Obdan, H. Design Methodology of Series Resonant Half Bridge Inverter for Induction Cooker. *IEEE Access* **2023**, *11*, 135476–135492. [CrossRef] [CrossRef]
10. Ozturk, M.; Aslan, S.; Altintas, N.; Sinirlioglu, S. Comparison of Induction Cooker Power Converters. In Proceedings of the 2018 6th International Conference on Control Engineering & Information Technology (CEIT), Istanbul, Turkey, 25–27 October 2018. [CrossRef]
11. Omori, H.; Nakaoka, M. New Single-Ended Resonant Inverter Circuit and System for Induction-Heating Cooking Apparatus. *Int. J. Electron.* **1989**, *67*, 277–296. [CrossRef] [CrossRef]
12. Koertzen, H.W.; van Wyk, J.D.; Ferreira, J.A. Design of the Half-Bridge, Series Resonant Converter for Induction Cooking. In Proceedings of the PESC '95—Power Electronics Specialist Conference, Atlanta, GA, USA, 18–22 June 1995; Volume 2, pp. 729–735. [CrossRef]
13. Pérez-Tarragona, M.; Sarnago, H.; Lucía, Ó.; Burdío, J.M. High Performance Full-Bridge Multi-Inverter Featuring 900-V SiC Devices for Domestic Induction Heating Applications. *EPE J. Eur. Power Electron. Drives J.* **2017**, *27*, 143–152. [CrossRef] [CrossRef]
14. Ngoc, H. P.; Fujita, H.; Ozaki, K.; Uchida, N. Phase Angle Control of High-Frequency Resonant Currents in a Multiple Inverter System for Zone-Control Induction Heating. *IEEE Trans. Power Electron.* **2011**, *26*, 3357–3366. [CrossRef] [CrossRef]
15. Guillen, P.; Sarnago, H.; Lucia, O.; Burdio, J.M. Multi-Output Resonant Power Converters for Domestic Induction Heating. In Proceedings of the IECON 2020 The 46th Annual Conference of the IEEE Industrial Electronics Society, Singapore, 18–21 October 2020; pp. 4320–4327. [CrossRef]
16. Sarnago, H.; Lucía, Ó.; Mediano, A.; Burdío, J.M. A Class-E Direct AC–AC Converter with Multicycle Modulation for Induction Heating Systems. *IEEE Trans. Ind. Electron.* **2014**, *61*, 2521–2530. [CrossRef] [CrossRef]
17. Hobson, L.; Tebb, D.W.; Turnbull, D. Dual-Element Induction Cooking Unit Using Power MOSFETs. *Int. J. Electron.* **1985**, *59*, 747–757. [CrossRef] [CrossRef]
18. Dawson, F.P.; Jain, P. A Comparison of Load Commutated Inverter Systems for Induction Heating and Melting Applications. *IEEE Trans. Power Electron.* **1991**, *6*, 430–441. [CrossRef] [CrossRef]
19. Pham, H.N.; Fujita, H.; Ozaki, K.; Uchida, N. Dynamic Analysis and Control for Resonant Currents in a Zone-Control Induction Heating System. *IEEE Trans. Power Electron.* **2013**, *28*, 1297–1307. [CrossRef] [CrossRef]
20. Burdío, J.M.; Monterde, F.; García, J.R.; Barragán, L.A.; Martínez, A. A Two-Output Series-Resonant Inverter for Induction-Heating Cooking Appliances. *IEEE Trans. Power Electron.* **2005**, *20*, 815–822. [CrossRef] [CrossRef]
21. Forest, F.; Laboure, E.; Costa, F.; Gaspard, J.Y. Principle of a Multi-Load/Single Converter System for Low Power Induction Heating. *IEEE Trans. Power Electron.* **2000**, *15*, 223–230. [CrossRef] [CrossRef]
22. Sarnago, H.; Saoudi, M.; Mediano, A.; Puyal, D.; Lucía, Ó. Hybrid Full/Half Wave Inverter Designed for Low Cost Induction Heating Appliances. In Proceedings of the IECON 2011—37th Annual Conference of the IEEE Industrial Electronics Society, Melbourne, Australia, 7–10 November 2011; pp. 2539–2544. [CrossRef]
23. Sarnago, H.; Lucía, Ó.; Burdío, J.M. FPGA-Based Resonant Load Identification Technique for Flexible Induction Heating Appliances. *IEEE Trans. Ind. Electron.* **2018**, *65*, 9421–9428. [CrossRef] [CrossRef]
24. Lucía, Ó.; Acero, J.; Carretero, C.; Burdío, J.M. Induction Heating Appliances: Toward More Flexible Cooking Surfaces. *IEEE Ind. Electron. Mag.* **2013**, *7*, 35–47. [CrossRef] [CrossRef]
25. Acero, J.; Burdío, J.M.; Barragán, L.A.; Navarro, D.; Alonso, R.; Ramón, J.R.; Monterde, F.; Hernández, P.; Llorente, S.; Garde, I. Domestic Induction Appliances. *IEEE Ind. Appl. Mag.* **2010**, *16*, 39–47. [CrossRef] [CrossRef]

26. Sarnago, H.; Lucía, Ó.; Pérez-Tarragona, M.; Burdío, J.M. Dual-Output Boost Resonant Full-Bridge Topology and Its Modulation Strategies for High-Performance Induction Heating Applications. *IEEE Trans. Ind. Electron.* **2016**, *63*, 3554–3561. [CrossRef] [CrossRef]
27. Sarnago, H.; Lucía, Ó.; Mediano, A.; Burdío, J.M. Design and Implementation of a High-Efficiency Multiple-Output Resonant Converter for Induction Heating Applications Featuring Wide Bandgap Devices. *IEEE Trans. Power Electron.* **2014**, *29*, 2539–2549. [CrossRef] [CrossRef]
28. Lucía, Ó.; Carretero, C.; Burdío, J.M.; Acero, J.; Almazán, F. Multiple-Output Resonant Matrix Converter for Multiple Induction Heaters. *IEEE Trans. Ind. Appl.* **2012**, *48*, 1387–1396. [CrossRef] [CrossRef]
29. Saoudi, M.; Puyal, D.; Sarnago, H.; Antón, D.; Mediano, A. A New Multiple Coils Topology for Domestic Induction Cooking System. In Proceedings of the IECON 2011—37th Annual Conference of the IEEE Industrial Electronics Society, Melbourne, Australia, 7–10 November 2011. [CrossRef]
30. Papani, S.K.; Neti, V.; Murthy, B.K. Dual Frequency Inverter Configuration for Multiple-Load Induction Cooking Application. *IET Power Electron.* **2015**, *8*, 591–601. [CrossRef] [CrossRef]
31. Khatroth, S.; Shunmugam, P. Cascaded Full-Bridge Resonant Inverter Configuration for Different Material Vessel Induction Cooking. *IET Power Electron.* **2020**, *13*, 4428–4438. [CrossRef] [CrossRef]
32. Burdío, J.M.; Barragán, L.A.; Monterde, F.; Navarro, D.; Acero, J. Asymmetrical Voltage-Cancellation Control for Full-Bridge Series Resonant Inverters. *IEEE Trans. Power Electron.* **2004**, *19*, 461–469. [CrossRef] [CrossRef]
33. Sarnago, H.; Burdío, J.M.; Lucía, Ó. High-Performance and Cost-Effective ZCS Matrix Resonant Inverter for Total Active Surface Induction Heating Appliances. *IEEE Trans. Power Electron.* **2019**, *34*, 117–125. [CrossRef] [CrossRef]
34. Sarnago, H.; Guillén, P.; Burdío, J.M.; Lucía, Ó. Multiple-Output ZVS Resonant Inverter Architecture for Flexible Induction Heating Appliances. *IEEE Access* **2019**, *7*, 157046–157056. [CrossRef] [CrossRef]
35. Ozturk, M.; Altintas, N. Multi-Output AC–AC Converter for Domestic Induction Heating. *Electr. Eng.* **2023**, *105*, 297–316. [CrossRef] [CrossRef]
36. Rehm, F.; Hiller, M. A Non-Resonant Multi-Output Half-Bridge Inverter for Flexible Cooking Surfaces. In Proceedings of the 2023 11th International Conference on Power Electronics and ECCE Asia (ICPE 2023—ECCE Asia), Jeju Island, Republic of Korea, 22–25 May 2023; pp. 2591–2597. [CrossRef]
37. Raeber, M.; Amiras, P.; Heinzelmann, A. Analysis on the Use of Non-Resonant Inverters in Single-Phase Induction Heating Applications. In Proceedings of the IECON 2020 The 46th Annual Conference of the IEEE Industrial Electronics Society, Singapore, 18–21 October 2020; pp. 4315–4319. [CrossRef]
38. Jordan, J.; Esteve, V.; Sanchis-Kilders, E.; Dede, E.J.; Maset, E.; Ejea, J.B.; Ferreres, A. A Comparative Performance Study of a 1200 V Si and SiC MOSFET Intrinsic Diode on an Induction Heating Inverter. *IEEE Trans. Power Electron.* **2014**, *29*, 2550–2562. [CrossRef] [CrossRef]
39. Aslan, S.; Ozturk, M.; Altintas, N. A Comparative Study of SiC and Si Power Devices in Induction Cookers. In Proceedings of the 2018 5th International Conference on Electrical and Electronic Engineering (ICEEE), Istanbul, Turkey, 3–5 May 2018; pp. 297–301. [CrossRef]
40. Sarnago, H.; Burdío, J.M.; Lucía, Ó. High-Frequency GaN-Based Induction Heating Versatile Module for Flexible Cooking Surfaces. In Proceedings of the 2019 IEEE Applied Power Electronics Conference and Exposition (APEC), Anaheim, CA, USA, 17–21 March 2019; pp. 448–452. [CrossRef]
41. Jang, E.; Kwon, M.J.; Park, S.M.; Ahn, H.M.; Lee, B.K. Analysis and Design of Flexible-Surface Induction-Heating Cooktop with GaN-HEMT-Based Multiple Inverter System. *IEEE Trans. Power Electron.* **2022**, *37*, 12865–12876. [CrossRef] [CrossRef]
42. Erken, A.; Obdan, A.H. Examining the Optimal Use of WBG Devices in Induction Cookers. *Appl. Sci.* **2023**, *13*, 12517. [CrossRef] [CrossRef]
43. Lucía, Ó.; Burdío, J.M.; Millan, I.; Acero, J.; Puyal, D. Load-Adaptive Control Algorithm of Half-Bridge Series Resonant Inverter for Domestic Induction Heating. *IEEE Trans. Ind. Electron.* **2009**, *56*, 3106–3116. [CrossRef] [CrossRef]